PROCEEDINGS OF THE 22nd INTERNATIONAL SYMPOSIUM ON APPLICATION OF LASER AND IMAGING TECHNIQUES TO FLUID MECHANICS 2026

KEYNOTES

AERODYNAMICS

AERODYNAMICS AND FLOW CONTROL

ARTIFICIAL LEARNING METHODS

BACKGROUND ORIENTED SCHLIEREN

BIOMEDICAL FLOWS

BOUNDARY LAYERS

COMBUSTION

DEFOCUSED PARTICLE TRACKING

EVENT-BASED IMAGING

FILTERED RAYLEIGH SCATTERING

FORCE AND PRESSURE FROM PIV DATA

HEAT TRANSFER AND THERMODYNAMIC PHENOMENA

HIGH-SPEED VELOCIMETRY

IMAGING

JETS

LIF/PLIF TECHNIQUE

MEASUREMENT OF WALL SHEAR STRESS

MICRO-SCALE PIV AND MICROFLUIDICS

NOVEL MEASUREMENT TECHNIQUES

PARTICLE / SPRAY MEASUREMENT TECHNIQUES

PIV AND LIF

PIV APPLICATIONS

PIV DATA ASSIMILATION

PIV UNCERTAINTY QUANTIFICATION AND PERFORMANCE

PTV TECHNIQUES

SHOCKS AND COMPRESSIBLE FLOWS

SPRAYS

TURBULENCE

TWO-PHASE FLOWS

VOLUMETRIC PIV/PTV

VOLUMETRIC PIV/PTV APPLICATIONS

WAKES

ISBN 978-989-53637-2-8

KEYNOTES

Exploring Turbulent Dispersion and Urban Aerodynamics via PIV and PLIF
Christina Vanderwel

Tracing the footprints in high-speed flows via fast PSP & TSP:
from flow instability to symmetry
Di Peng

Recent Developments in Near-Wall Measurements
Philippe Bardet

On the problem of diffusivity in biological materials: estimation of diffusion coefficients via X-ray radiography

E. Medolago, M. Santini*, S. Fest-Santini, G.E. Cossali

Department of Engineering and Applied Sciences, University of Bergamo, Italy
*Corresponding author: maurizio.santini@unibg.it

Keywords: diffusion coefficient, X-ray radiography, mass transfer, biological tissue, FFPE tissue, tissue processing, porous media.

ABSTRACT

The processing of histological samples, particularly biopsies, is a pivotal step in the medical histopathology, as it prepares the sample for the subsequent microscopic examination. During this examination, the morphological, functional and molecular characteristics of the tissue withdrawn from the patient are investigated. Histological evaluation of biopsies is a cornerstone of daily medical diagnosis, staging and grading of many diseases, especially cancers. All the phases of the specimen preparation process require the diffusion of a solvent within the sample mass. Therefore, having reliable knowledge regarding the diffusion in biological materials is of crucial importance. This article presents an experimental technique to determine the diffusion coefficient in biological specimens. This key physical quantity provides significant information about the rate at which a substance spreads within a given medium. The objective was accomplished through the acquisition of a sequence of radiographic images of biological samples having different geometries immersed in processing solvents. As X-ray attenuation is proportional to the solvent's concentration, changes in radiograph intensity over time reflect the diffusion of the substance in the irradiated sample. The intensity data were therefore fitted using analytically derived mathematical models for the diffusion coefficients estimation.

1. Introduction

Since the late 19th century, Formalin-Fixed Paraffin-Embedded (FFPE) tissue has been the established method for preserving clinical specimens for histopathological examination and archiving in routine histopathological and clinical practice. FFPE tissue samples detain a crucial role in histopathology for diagnostic, therapeutic and research purposes, enabling microscopic morphological examination and molecular analysis (Magaki et al., 2018; Kokkat et al., 2013). In particular, their examination is a mainstay in cancer diagnosis and treatment, giving also fundamental information for precision medicine and immunotherapy. Furthermore, it is widely considered as the gold standard for the diagnosis of many other diseases, such as autoimmune and inflammatory diseases, infections, and skin diseases (Zhu et al., 2024; Villanacci et al., 2020).

FFPE techniques consist of multiple sequential steps, including tissue acquisition, fixation, dehydration, clearing, paraffin embedding, sectioning, and staining (Spencer et al., 2012). In general, biological tissues are multi-compartmental, heterogeneous media (Sen & Basser, 2005; Posnansky & Shah, 2008), demonstrating different refractive indices. The aim of tissue clearing is to achieve uniform refractive indices and to minimize light scattering (Mai & Lu, 2024). To this end, histological specimens are submerged in different organic and aqueous solvents until saturation occurs. These processes are generally performed by automatic processors that adhere to standardized protocols, which rely on empirical timing. In this way, specimens can be under or over-treated and the optimal quality is no longer guaranteed. Each stage in histological sample processing, especially when conducted sub-optimally, has the ability to generate artifacts in tissue sections (McInnes, 2005; Ekundina & Eze, 2015; Taqi et al., 2018) and to introduce errors in sample preparation. This has a potential detrimental effect on histopathological analysis (Agrawal et al., 2018; Engel & Moore, 2011), which in turn can affect the accuracy of the medical diagnosis. Just after the extraction and the stabilization in buffered formalin of the biopsy, the dehydration phase occurs. During this phase, the sample is treated with a series of alcoholic solutions with increasing concentrations, starting from 70% to 100%. Dehydration is very critical, as it can persist for a long time and strong concentration gradients are established during this period. These gradients have the potential to distort the sample in terms of histological and cellular elements (Spencer et al., 2012). It is therefore essential to ensure that the duration of this step is properly determined. Herefor, the diffusion of 70% alcohol was investigated during the experiments.

Examining the diffusion phenomenon in histological samples enables the determination of the appropriate timing of each stage of sample preparation, with the estimation of the diffusion coefficient as a crucial endpoint. This quantity, alternatively referred to as diffusivity, quantifies the ease with which a molecule diffuses within a given medium. In the literature, few techniques have been reported, which are too indirect, more or less extensible (Bauer et al., 2016; Lerch et al., 2017, 2019), too complex or based on limited available apparatus and infrastructures (Le Houx et al., 2023) or related to distinct applications, such as the Diffusion-Weighted Imaging (DWI), which enables the in-vivo determination of the so-called Apparent Diffusion Coefficient (ADC).

A novel methodology for the determination of diffusivity in biological materials was previously implemented (Santini et al., 2024) and patent pending (Santini et al., 2023). In this paper, this methodology has been further refined and extended to accommodate samples with different geometries. In particular, diffusion coefficients were estimated for spherical, cylindrical, and cuboid-shaped pork liver samples, the three main shapes of histological samples, immersed in 70% ethanol. The obtained results were used to analyze the impact of the sample's shape and geometrical features on the diffusion coefficient estimates.

2. Materials and methods

2.1. Experimental setup

For the experiments, spherical, cylindrical, and cuboid-shaped resections of porcine livers were used. These samples had already been stabilized in buffered formalin for $24\ h$ or $48\ h$. Each tissue was placed in a $50\ mL$ Falcon tube in which the solvent (alcohol 70%) was injected by means of a $20\ mL$ syringe. The sample was then exposed to the ionizing radiation in a custom microCT facility by a microfocus X-ray source with conical emission (Hamamatsu X-ray Tube Unit L11902), operating at $120\ kV$ and $22\ \mu A$ (target current). The radiographs were acquired at $1.25\ Hz$ for a total time of $30\ min$, recorded and digitalized as TIFF images by a Varex Imaging's 1512 CMOS flat panel X-ray detector with a pixel pitch of $74.8\ \mu m$ and a pixel matrix of 1944×1536 pixels. Radiographs were acquired using a 2×2 pixel binning, resulting in an image size of 972×768 pixels, with an acquisition time of $650\ ms$. For detailed information regarding X-ray microtomography and instrumentation refer to Santini et al. (2013).
During acquisition, the radiographs were corrected for detector charge accumulation ("dark-field") and "bright-field" normalized. The resolution of the acquired radiographs varies from 13 to 22 $\mu m/pixel$ based on the source-to-object distance, which was adapted to specimen dimensions. The biological sample was fully immersed in the alcoholic solution and maintained in a fixed position (Fig. 1), realistically simulating the dehydration phase. Both samples and alcoholic solution reached thermal equilibrium before starting the experiments. A digital sensor was used to monitor the experimental ambient conditions (temperature and humidity) at one-minute intervals.

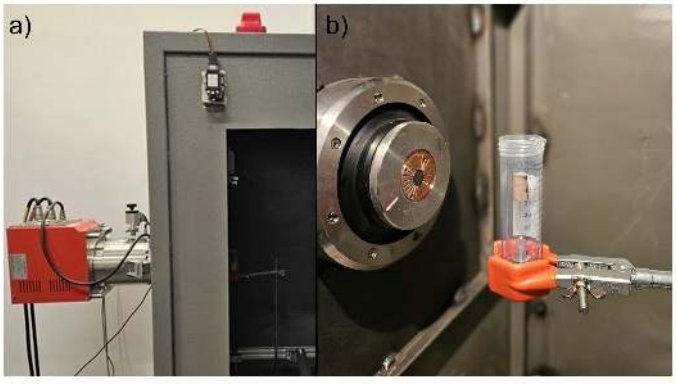

Figure 1. The figure shows: a) the X-ray source and b) the setup used for sample positioning and holding.

Following acquisition, the radiographs were processed using an algorithm developed in MATLAB®. The algorithm clustered the pixels in the sample area into multiple square Regions Of Interest (ROIs) of 40x40 pixels, where the mean intensity value was computed. This facilitated the intensity variation in each ROI over time to be captured. As changes in X-ray attenuation are di-

rectly related to the changes in solvent's concentration, the time dependent diffusion process can be observed and analyzed. The processed radiographs were thus used for the estimation of the diffusion coefficient.

2.2. Mathematical models

Assuming material isotropy and homogeneity, and considering uniform and constant effective diffusion coefficient, the diffusion equation in cartesian (Eq. (1)), cylindrical (Eq. (2)) and spherical (Eq. (3)) coordinates can be written as follows:

$$\frac{\partial \rho}{\partial t} = D_{eff}\left(\frac{\partial^2 \rho}{\partial x^2} + \frac{\partial^2 \rho}{\partial y^2} + \frac{\partial^2 \rho}{\partial z^2}\right) \tag{1}$$

$$\frac{\partial \rho}{\partial t} = D_{eff}\left(\frac{\partial^2 \rho}{\partial r^2} + \frac{1}{r}\frac{\partial \rho}{\partial r} + \frac{\partial^2 \rho}{\partial z^2}\right) \tag{2}$$

$$\frac{\partial \rho}{\partial t} = D_{eff}\frac{1}{r^2}\frac{\partial}{\partial r}\left(r^2\frac{\partial \rho}{\partial r}\right) \tag{3}$$

where D_{eff} is the effective diffusion coefficient and ρ is the concentration of the diffusing substance. Eq. (2) accounts for axial symmetry, while Eq. (3) accounts for spherical symmetry. The initial conditions (IC) and the boundary conditions (BC) can be imposed by considering an initial uniform value (ρ_0) for the concentration of the diffusing substance within the sample volume Ω as IC, and a uniform and constant value (ρ_1) of the concentration of the diffusing substance on the sample boundaries $\partial\Omega$ as Dirichlet BC.

By defining the new dimensionless variable:

$$\chi = \left(\frac{\rho - \rho_1}{\rho_0 - \rho_1}\right) \tag{4}$$

Eq. (1), Eq. (2), and Eq. (3) can be rewritten respectively as:

$$\frac{\partial \chi}{\partial t} = D_{eff}\left(\frac{\partial^2 \chi}{\partial x^2} + \frac{\partial^2 \chi}{\partial y^2} + \frac{\partial^2 \chi}{\partial z^2}\right) \tag{5}$$

$$\frac{\partial \chi}{\partial t} = D_{eff}\left(\frac{\partial^2 \chi}{\partial r^2} + \frac{1}{r}\frac{\partial \chi}{\partial r} + \frac{\partial^2 \chi}{\partial z^2}\right) \tag{6}$$

$$\frac{\partial \chi}{\partial t} = D_{eff}\frac{1}{r^2}\frac{\partial}{\partial r}\left(r^2\frac{\partial \chi}{\partial r}\right) \tag{7}$$

The IC and BC become:

$$\chi = 1 \; in \; \Omega, \; t = 0 \tag{8}$$

$$\chi = 0 \; on \; \partial\Omega, \; t > 0 \tag{9}$$

The symmetry conditions are:

$$\left(\frac{\partial \chi}{\partial x}\right)_{x=0} = 0; \; \left(\frac{\partial \chi}{\partial y}\right)_{y=0} = 0; \; \left(\frac{\partial \chi}{\partial z}\right)_{z=0} = 0; \; t > 0 \tag{10}$$

$$\left(\frac{\partial \chi}{\partial r}\right)_{r=0} = 0; \; \left(\frac{\partial \chi}{\partial z}\right)_{z=0} = 0; \; t > 0 \tag{11}$$

$$\left(\frac{\partial \chi}{\partial r}\right)_{r=0} = 0; \; t > 0 \tag{12}$$

for the cuboid-shaped, cylindrical, and spherical samples, respectively (assuming a perfect sample geometry).
Eq. (5), Eq. (6), and Eq. (7) can be solved employing the method of separation of variables (P. D. Moon, 1988). The obtained general solutions (Luikov, 2012; Crank, 1979), written in series form, are respectively:

$$\chi(x, y, z, t) = \sum_{n=0}^{\infty} \sum_{m=0}^{\infty} \sum_{k=0}^{\infty} a_{n,m,k} e^{-D_{eff} \lambda_{n,m,k}^2 t} \cos(\gamma_n x) \cos(\mu_m y) \cos(\omega_k z) \tag{13}$$

$$\chi(r, z, t) = \sum_{n=0}^{\infty} \sum_{k=0}^{\infty} a_{n,k} e^{-D_{eff} \lambda_{k,n}^2 t} J_0(\phi_n r) \cos\left(\left(\frac{\pi}{2} + k\pi\right) \frac{z}{Z_0}\right) \tag{14}$$

$$\chi(r, t) = \sum_{n=1}^{\infty} a_n e^{-D_{eff} \lambda_n^2 t} \frac{\sin(\lambda_n r)}{\lambda_n r} \tag{15}$$

with:

$$\lambda_{n,m,k}^2 = \gamma_n^2 + \mu_m^2 + \omega_k^2 = \left(\frac{\pi}{2X_0} + \frac{n\pi}{X_0}\right)^2 + \left(\frac{\pi}{2Y_0} + \frac{m\pi}{Y_0}\right)^2 + \left(\frac{\pi}{2Z_0} + \frac{k\pi}{Z_0}\right)^2 \tag{16}$$

$$\lambda_{k,n}^2 = \left(\frac{\pi}{2Z_0} + \frac{k\pi}{Z_0}\right)^2 + \phi_n^2, \; \phi_n = \frac{j_n}{R_0} \tag{17}$$

$$\lambda_n = \frac{n\pi}{R_0} \tag{18}$$

where:

- J_0 is the zero-order Bessel function of the first type and j_n are its zeros;
- X_0, Y_0 and Z_0 in Eq. (16) represent the half-width, half-depth, and half-height of a cuboid-shaped sample, respectively;
- R_0 in Eq. (17) is the external radius of a cylindrical sample, while Z_0 is its half-height;
- R_0 in Eq. (18) is the external radius of a spherical sample;
- $n, m, k \in \mathbb{N}$.

The coefficients $a_{n,m,k},\ a_{n,k}$, and a_n in Eq. (13), Eq. (14), and Eq. (15), respectively, can be identified by satisfying the IC reported in Eq. (8). In particular, exploiting the orthogonality of cosine, Bessel's, and sinus functions (Olver, 2010), these coefficients are given by the following:

$$a_{n,m,k} = (-1)^{n+m+k} \frac{8}{\left(\frac{\pi}{2} + n\pi\right)\left(\frac{\pi}{2} + m\pi\right)\left(\frac{\pi}{2} + k\pi\right)} \tag{19}$$

$$a_{n,k} = (-1)^{k} \frac{4}{j_n \left(\frac{\pi}{2} + k\pi\right) J_1(j_n)} \tag{20}$$

$$a_n = 2(-1)^{n+1} \tag{21}$$

where J_1 in Eq. (20) is the first-order Bessel function of the first type.
As anticipated, since the attenuation of the detected X-ray beam was directly related to the concentration of the diffusing substance, the intensity values contained in the acquired X-ray images can be used to estimate the effective diffusion coefficient D_{eff}.

In this perspective, Lambert-Beer law can be considered:

$$dI = -\mu\rho I d\xi \tag{22}$$

where I is the intensity of the beam passing through a thickness $d\xi$ and μ is the mass attenuation coefficient. Assuming the local attenuation coefficient μ as constant, after integration, Eq. (22) yields:

$$\frac{I_u}{I_0} = e^{-\mu \int_{\xi_1}^{\xi_2} \rho(\xi,t) d\xi} \tag{23}$$

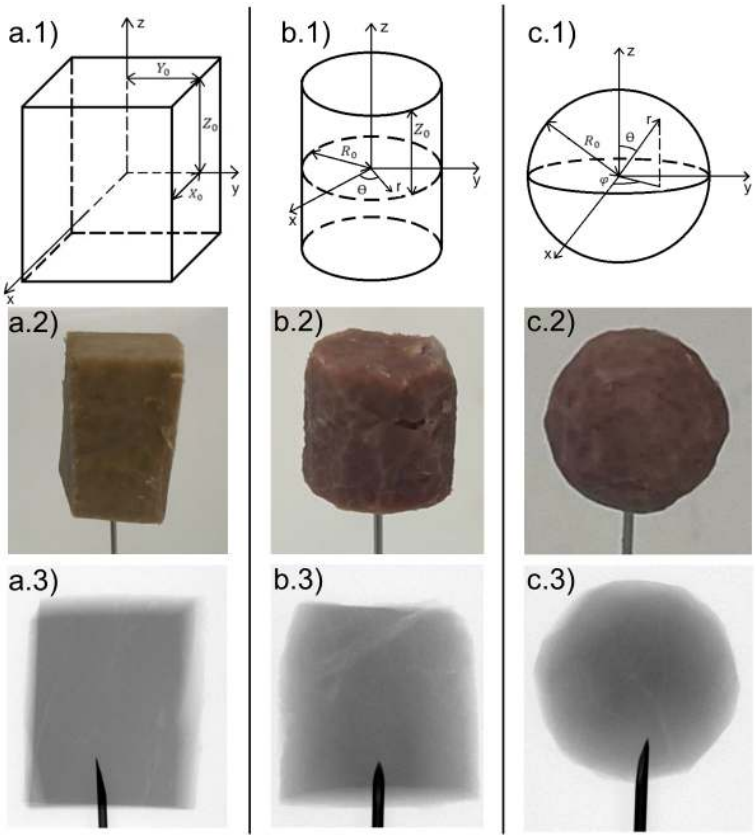

Figure 2. Geometry, dimensions and related coordinates system for each shape considered: a.1) cuboid, b.1) cylinder, and c.1) sphere. Pork liver samples (oblique angle view): a.2) cuboid-shaped, b.2) cylindrical, and c.2) spherical. Radiographic image of the samples: a.3) cuboid-shaped, b.3) cylindrical, and c.3) spherical.

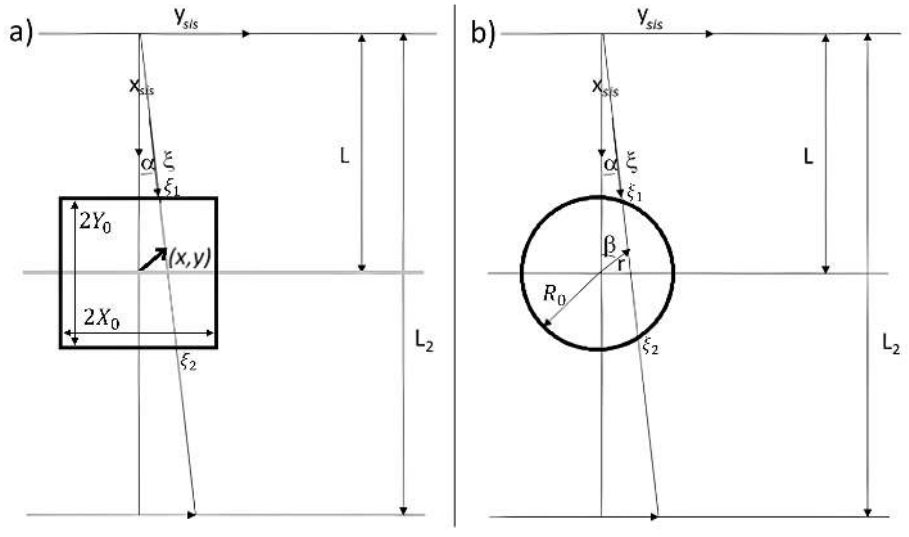

Figure 3. Schematic representation of the acquisition system at the mid-plane of the sample. The related coordinates, the spatial coordinate of the X-ray beam (conical emission) and the coordinate system of the sample are shown for: a) cuboid-shaped samples, b) cylindrical and spherical samples. L represents the source-to-object distance (SOD), while L_2 is the source-to-detector distance (SDD).

where ξ represents the spatial coordinate directed as the X-ray beam (Fig. 3), I_0 is the intensity of the beam entering the biological sample and I_u is the intensity of the attenuated beam leaving the sample. Thus, the absorption a for any X-ray beam passing through the sample mass is given by:

$$a\left(\xi_1, \xi_2, t\right) = \int_{\xi_1}^{\xi_2} \rho\left(\xi, t\right) d\xi \tag{24}$$

It is now possible to notice that Eq. (4) can be rearranged as:

$$\rho = \left(\rho_0 - \rho_1\right)\chi + \rho_1 \tag{25}$$

then the previous integral becomes:

$$\int_{\xi_1}^{\xi_2} \rho\left(\xi, t\right) d\xi = \left(\rho_0 - \rho_1\right) \int_{\xi_1}^{\xi_2} \chi\left(\xi, t\right) d\xi + \rho_1 \int_{\xi_1}^{\xi_2} d\xi. \tag{26}$$

Since x, y, z, and r are all functions of the coordinate ξ, and recalling the general solutions in Eq. (13), Eq. (14) and Eq. (15), the integrals of χ along any X-ray beam can be rewritten as follows:

$$\int_{\xi_1}^{\xi_2} \chi\left(\xi, t\right) d\xi = \sum_{n=0}^{\infty}\sum_{m=0}^{\infty}\sum_{k=0}^{\infty} a_{n,m,k} e^{-D_{eff}\lambda_{n,m,k}^2 t} \int_{\xi_1}^{\xi_2} \cos\left(\gamma_n x(\xi)\right)\cos\left(\mu_m y(\xi)\right)\cos\left(\omega_k z(\xi)\right) d\xi \tag{27}$$

$$\int_{\xi_1}^{\xi_2} \chi\left(\xi, t\right) d\xi = \sum_{n=0}^{\infty}\sum_{k=0}^{\infty} a_{n,k} e^{-D_{eff}\lambda_{k,n}^2 t} \int_{\xi_1}^{\xi_2} J_0(\phi_n r(\xi)) \cos\left(\left(\frac{\pi}{2} + k\pi\right)\frac{z(\xi)}{Z_0}\right) d\xi \tag{28}$$

$$\int_{\xi_1}^{\xi_2} \chi\left(\xi, t\right) d\xi = \sum_{n=1}^{\infty} a_n e^{-D_{eff}\lambda_n^2 t} \int_{\xi_1}^{\xi_2} \frac{sin\left(\lambda_n r(\xi)\right)}{\lambda_n r(\xi)} d\xi \tag{29}$$

then, the X-ray absorptions can be rewritten as:

$$a\left(t\right) = \left(\rho_0 - \rho_1\right)\sum_{n=0}^{\infty}\sum_{m=0}^{\infty}\sum_{k=0}^{\infty} e^{-D_{eff}\lambda_{n,m,k}^2 t} C_{n,m,k}(\xi_1, \xi_2) + \rho_1(\xi_2 - \xi_1) \tag{30}$$

$$a\left(t\right) = \left(\rho_0 - \rho_1\right)\sum_{n=0}^{\infty}\sum_{k=0}^{\infty} e^{-D_{eff}\lambda_{k,n}^2 t} C_{n,k}(\xi_1, \xi_2) + \rho_1(\xi_2 - \xi_1) \tag{31}$$

$$a\left(t\right) = \left(\rho_0 - \rho_1\right)\sum_{n=1}^{\infty} e^{-D_{eff}\lambda_n^2 t} C_n(\xi_1, \xi_2) + \rho_1(\xi_2 - \xi_1) \tag{32}$$

for cuboid-shaped, cylindrical, and spherical samples, respectively; where:

$$C_{n,m,k}(\xi_1,\xi_2) = a_{n,m,k}\int_{\xi_1}^{\xi_2}\cos\left(\gamma_n x(\xi)\right)\cos\left(\mu_m y(\xi)\right)\cos\left(\omega_k z(\xi)\right)d\xi \tag{33}$$

$$C_{n,k}(\xi_1,\xi_2) = a_{n,k}\int_{\xi_1}^{\xi_2} J_0(\phi_n r(\xi))\cos\left(\left(\frac{\pi}{2}+k\pi\right)\frac{z(\xi)}{Z_0}\right)d\xi \tag{34}$$

$$C_n(\xi_1,\xi_2) = a_n\int_{\xi_1}^{\xi_2}\frac{sin\left(\lambda_n r(\xi)\right)}{\lambda_n r(\xi)}d\xi \tag{35}$$

Now, it is convenient to define the following quantity:

$$Y\left(t\right) = ln\left(\frac{I_u(t)}{I_u(0)}\right) \tag{36}$$

from which:

$$Y\left(t\right) = \ ln\left(\frac{I_u\left(t\right)}{I_u\left(0\right)}\right) = \ ln\left(\frac{I_0 e^{-\mu a(t)}}{I_0 e^{-\mu a(0)}}\right) = \ \mu\left[a\left(0\right) - \ a\left(t\right)\right] \tag{37}$$

where $I_u(t)$ is the intensity of the X-ray beam exiting the histological sample for any given time $t > 0$, while $I_u(0)$ is the same intensity measured at $t = 0$.
It follows that Eq. (30), Eq. (31) and Eq. (32) yield, respectively:

$$Y\left(t\right) = d^*_{0_{n,m,k}} + \sum_{n=0}^{\infty}\sum_{m=0}^{\infty}\sum_{k=0}^{\infty} d^*_{n,m,k} e^{-D_{eff}\left[\left(\frac{\pi}{2X_0}+\frac{n\pi}{X_0}\right)^2+\left(\frac{\pi}{2Y_0}+\frac{m\pi}{Y_0}\right)^2+\left(\frac{\pi}{2Z_0}+\frac{k\pi}{Z_0}\right)^2\right]t} \tag{38}$$

$$Y\left(t\right) = \ d^*_{0_{n,k}} + \sum_{n=0}^{\infty}\sum_{k=0}^{\infty} d^*_{n,k} e^{-\ \frac{D_{eff}}{{R_0}^2}\ \left[\frac{1}{\varepsilon^2}\left(\frac{\pi}{2}+k\pi\right)^2+j_n^2\right]t} \tag{39}$$

$$Y\left(t\right) = d^*_{0_n} + \ \sum_{n=1}^{\infty} d^*_n e^{-D_{eff}\left(\frac{n\pi}{R_0}\right)^2 t} \tag{40}$$

where

$$d^*_{0_{n,m,k}} = \ \mu(\rho_0-\rho_1)\sum_{n=0}^{\infty}\sum_{m=0}^{\infty}\sum_{k=0}^{\infty} C_{n,m,k}(\xi_1,\xi_2)\ ;\ d^*_{n,m,k} = \ -\mu(\rho_0-\rho_1)\ C_{n,m,k}(\xi_1,\xi_2) \tag{41}$$

$$d^*_{0_{n,k}} = \mu(\rho_0 - \rho_1) \sum_{n=0}^{\infty} \sum_{k=0}^{\infty} C_{n,k}(\xi_1, \xi_2) \; ; \; d^*_{n,k} = -\mu(\rho_0 - \rho_1) \, C_{n,k}(\xi_1, \xi_2) \; ; \; \varepsilon = \frac{Z_0}{R_0} \tag{42}$$

$$d^*_{0_n} = \mu(\rho_0 - \rho_1) \sum_{n=1}^{\infty} C_n(\xi_1, \xi_2) \; ; \; d^*_n = -\mu(\rho_0 - \rho_1) \, C_n(\xi_1, \xi_2) \tag{43}$$

There exists a finite time interval between the injection of the alcoholic solution into the Falcon containing the biological sample and the initiation of radiographic acquisition, resulting in a discrepancy between the time at which the measurement starts and the onset of diffusion. In order to consider this time interval, it is possible to apply the following substitution:

$$t = t' + t_0 \tag{44}$$

where t' is the time measured starting from the initiation of radiographic acquisition, while t_0 is a constant that considers the interval of time mentioned above. Applying this substitution, Eq. (38), Eq. (39) and Eq. (40) yield:

$$Y(t) = c^*_{0_{n,m,k}} + \sum_{n=0}^{\infty} \sum_{m=0}^{\infty} \sum_{k=0}^{\infty} c^*_{n,m,k} e^{-D_{eff}\left[\left(\frac{\pi}{2X_0} + \frac{n\pi}{X_0}\right)^2 + \left(\frac{\pi}{2Y_0} + \frac{m\pi}{Y_0}\right)^2 + \left(\frac{\pi}{2Z_0} + \frac{k\pi}{Z_0}\right)^2\right] t'} \tag{45}$$

$$Y(t) = c^*_{0_{n,k}} + \sum_{n=0}^{\infty} \sum_{k=0}^{\infty} c^*_{n,k} e^{-\frac{D_{eff}}{{R_0}^2}\left[\frac{1}{\varepsilon^2}\left(\frac{\pi}{2} + k\pi\right)^2 + j_n^2\right] t'} \tag{46}$$

$$Y(t) = c^*_{0_n} + \sum_{n=1}^{\infty} c^*_n e^{-D_{eff}\left(\frac{n\pi}{R_0}\right)^2 t'} \tag{47}$$

where

$$c^*_{0_{n,m,k}} = d^*_{0_{n,m,k}}; \; c^*_{n,m,k} = d^*_{n,m,k} e^{-D_{eff}\left[\left(\frac{\pi}{2X_0} + \frac{n\pi}{X_0}\right)^2 + \left(\frac{\pi}{2Y_0} + \frac{m\pi}{Y_0}\right)^2 + \left(\frac{\pi}{2Z_0} + \frac{k\pi}{Z_0}\right)^2\right] t_0} \tag{48}$$

$$c^*_{0_{n,k}} = d^*_{0_{n,k}}; \; c^*_{n,k} = d^*_{n,k} e^{-\frac{D_{eff}}{{R_0}^2}\left[\frac{1}{\varepsilon^2}\left(\frac{\pi}{2} + k\pi\right)^2 + j_n^2\right] t_0} \tag{49}$$

$$c^*_{0_n} = d^*_{0_n}; \; c^*_n = d^*_n e^{-D_{eff}\left(\frac{n\pi}{R_0}\right)^2 t_0} \tag{50}$$

for cuboid-shaped, cylindrical and spherical samples respectively.

2.3. Fitting procedure

Diffusion coefficients were estimated using multiple exponential fitting of Eq. (45), Eq. (46), and Eq. (47) for cuboid-, cylindrical- and spherical-shaped samples, respectively, on the experimental $Y(t)$ values (Fig. (4)) computed in each ROI of the sample area obtained from the processed radiographic sequences. The fitting procedure was performed in MATLAB® via the non-linear least squares method, considering four terms of the series.

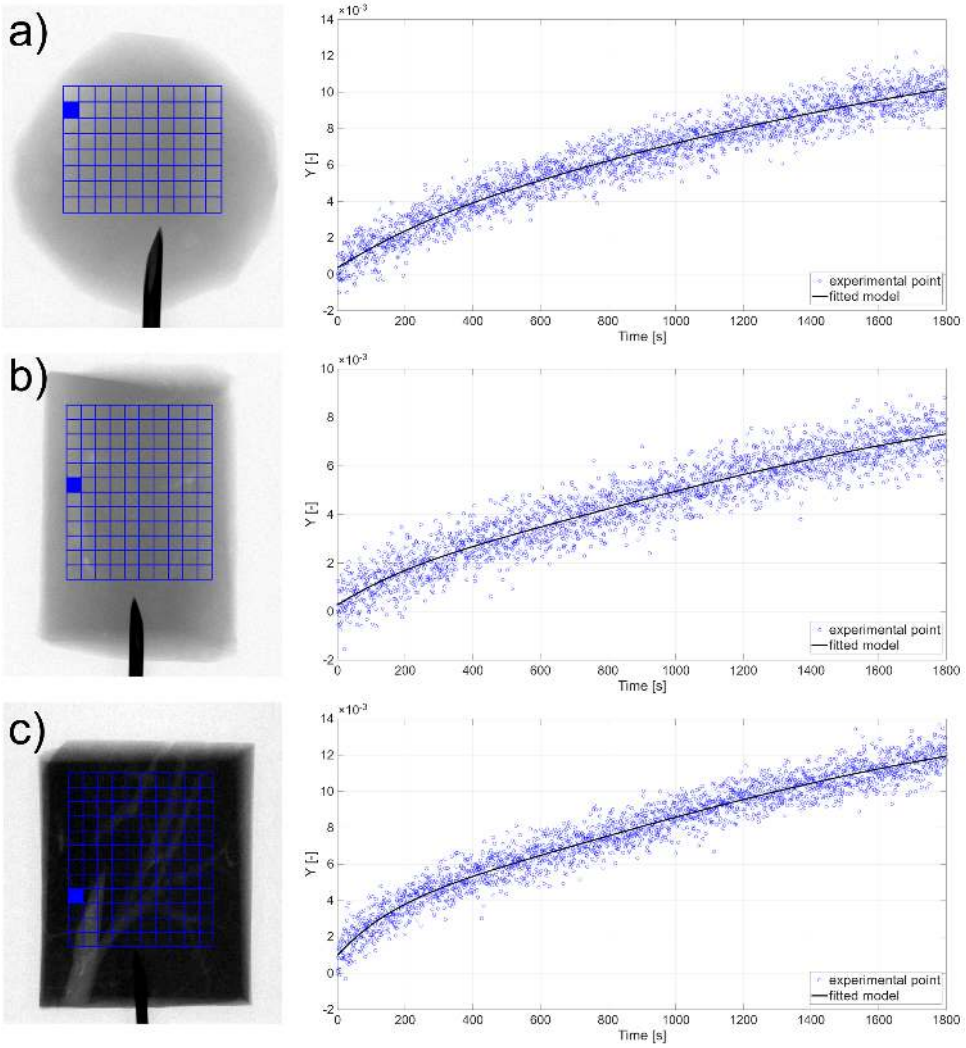

Figure 4. The figure shows the experimental data, the fitted analytical model and the related ROI for: a) a spherical sample, b) a cylindrical sample and c) a cuboid-shaped sample.

3. Results

Results were obtained for sixty-six different samples of pork liver (eleven for each shape and fixation timing, denoted as S_i, with $i = 1 : 11$) as effective diffusion coefficients estimated in each

ROI of the whole sample in the radiographic plane. Based on these estimates, mean effective diffusion coefficients and related standard deviations were computed. Three different values of sample surface-to-volume ratio (S/V) were selected to explore their effect on the D_{eff} estimation. The S/V values were determined by considering common sample sizes and taking spherical samples as a reference, given the limited possibility to adjust the surface-to-volume ratio for this geometry.
For samples S_1 to S_7, the sample surface-to-volume ratio was kept at $6.13\ cm^{-1}$ ($\pm\ 5\%$) (the reference value was obtained from the first spherical sample analyzed). The related mean effective diffusion coefficients and standard deviations are reported in Tables 1 and 2, and the resulting global values of D_{eff} are:

- $1.76 \times 10^{-9} \pm 0.55 \times 10^{-9}\ m^2/s$ and $1.82 \times 10^{-9} \pm 0.53 \times 10^{-9}\ m^2/s$ in spherical samples fixed for $24\ h$ and $48\ h$, respectively;
- $2.70 \times 10^{-9} \pm 0.42 \times 10^{-9}\ m^2/s$ and $2.66 \times 10^{-9} \pm 0.42 \times 10^{-9}\ m^2/s$ in cylindrical samples fixed for $24\ h$ and $48\ h$, respectively;
- $2.99 \times 10^{-9} \pm 0.41 \times 10^{-9}\ m^2/s$ and $2.73 \times 10^{-9} \pm 0.52 \times 10^{-9}\ m^2/s$ in cuboid-shaped samples fixed for $24\ h$ and $48\ h$, respectively.

For samples S_1 to S_6, the sample-to-solvent volume ratio (V_{sam}/V_{sol}) was kept constant at $1:50$. For samples S_7, this ratio was varied, increased up to $\sim\ 1:108$ for spherical specimens (where the solvent volume was basically lower given the lower samples volume) and decreased to $1:25$ for cylindrical and cuboid-shaped specimens (where the solvent volume was basically higher given the higher samples volume). No significant differences in the D_{eff} estimates with respect to variations in V_{sam}/V_{sol} were found.
For samples S_8 and S_9, the S/V was decreased to $4.83\ cm^{-1}$ ($\pm\ 5\%$) (reference value obtained from the first spherical sample analyzed for this series). The resulting mean effective diffusion coefficients and standard deviations are reported in Tables 3 and 4, and the global D_{eff} values are:

- $2.90 \times 10^{-9} \pm 0.90 \times 10^{-9}\ m^2/s$ and $3.11 \times 10^{-9} \pm 0.91 \times 10^{-9}\ m^2/s$ in spherical samples fixed for $24\ h$ and $48\ h$, respectively;
- $4.12 \times 10^{-9} \pm 0.75 \times 10^{-9}\ m^2/s$ and $4.20 \times 10^{-9} \pm 0.90 \times 10^{-9}\ m^2/s$ in cylindrical samples fixed for $24\ h$ and $48\ h$, respectively;
- $5.13 \times 10^{-9} \pm 0.83 \times 10^{-9}\ m^2/s$ and $4.66 \times 10^{-9} \pm 0.59 \times 10^{-9}\ m^2/s$ in cuboid-shaped samples fixed for $24\ h$ and $48\ h$, respectively.

For samples S_{10} and S_{11}, the S/V was increased to $7.41\ cm^{-1}$ ($\pm\ 5\%$) (reference value obtained from the first spherical sample analyzed for this series). The resulting mean effective diffusion coefficients and standard deviations are reported in Tables 5 and 6, and the global D_{eff} values are:

- $1.16 \times 10^{-9} \pm 0.37 \times 10^{-9}\ m^2/s$ and $1.26 \times 10^{-9} \pm 0.39 \times 10^{-9}\ m^2/s$ in spherical samples fixed for $24\ h$ and $48\ h$, respectively;
- $1.95 \times 10^{-9} \pm 0.33 \times 10^{-9}\ m^2/s$ and $1.72 \times 10^{-9} \pm 0.31 \times 10^{-9}\ m^2/s$ in cylindrical samples fixed for $24\ h$ and $48\ h$, respectively;
- $2.22 \times 10^{-9} \pm 0.26 \times 10^{-9}\ m^2/s$ and $2.00 \times 10^{-9} \pm 0.27 \times 10^{-9}\ m^2/s$ in cuboid-shaped samples fixed for $24\ h$ and $48\ h$, respectively.

The D_{eff} estimated in the ROIs within each sample and the related statistical metrics were also used to obtain color maps (Fig. (5)), where the colors reflect the homogeneity or deviation of the ROI effective diffusion coefficient from the average value computed for the entire sample.

Table 1. Table reporting mean effective diffusion coefficients and related standard deviations in $10^{-9}\ m^2/s$ for samples with $S/V = 6.13\ cm^{-1}$ $(\pm 5\%)$ fixed for $24h$ in neutral buffered formalin.

	Sphere	Cylinder	Cuboid
S_1	1.51 ± 0.55	2.53 ± 0.20	2.97 ± 0.32
S_2	1.59 ± 0.52	2.87 ± 0.74	3.25 ± 0.29
S_3	2.07 ± 0.77	2.62 ± 0.45	2.57 ± 0.35
S_4	1.79 ± 0.54	2.79 ± 0.27	3.04 ± 0.59
S_5	1.87 ± 0.49	2.73 ± 0.47	2.75 ± 0.50
S_6	1.74 ± 0.39	2.61 ± 0.31	3.23 ± 0.25
S_7	1.78 ± 0.56	2.73 ± 0.50	3.13 ± 0.59
Mean	1.76 ± 0.55	2.70 ± 0.42	2.99 ± 0.41

Table 2. Table reporting mean effective diffusion coefficients and related standard deviations in $10^{-9}\ m^2/s$ for samples with $S/V = 6.13\ cm^{-1}$ $(\pm 5\%)$ fixed for $48h$ in neutral buffered formalin.

	Sphere	Cylinder	Cuboid
S_1	1.65 ± 0.52	2.54 ± 0.32	3.17 ± 0.51
S_2	1.74 ± 0.56	2.85 ± 0.33	3.01 ± 0.68
S_3	1.63 ± 0.41	2.68 ± 0.57	2.82 ± 0.32
S_4	2.00 ± 0.71	2.46 ± 0.61	2.53 ± 0.50
S_5	1.95 ± 0.61	2.84 ± 0.45	2.25 ± 0.60
S_6	1.58 ± 0.42	2.59 ± 0.29	2.58 ± 0.61
S_7	2.17 ± 0.50	2.67 ± 0.37	2.74 ± 0.41
Mean	1.82 ± 0.53	2.66 ± 0.42	2.73 ± 0.52

Table 3. Table reporting mean effective diffusion coefficients and related standard deviations in $10^{-9}\ m^2/s$ for samples with $S/V = 4.83\ cm^{-1}$ $(\pm 5\%)$ fixed for $24h$ in neutral buffered formalin.

	Sphere	Cylinder	Cuboid
S_8	2.95 ± 0.87	4.21 ± 0.76	5.24 ± 0.97
S_9	2.84 ± 0.92	4.02 ± 0.73	5.02 ± 0.68
Mean	2.90 ± 0.90	4.12 ± 0.75	5.13 ± 0.83

Table 4. Table reporting mean effective diffusion coefficients and related standard deviations in $10^{-9}\ m^2/s$ for sample with $S/V = 4.83\ cm^{-1}$ $(\pm 5\%)$ fixed for $48h$ in neutral buffered formalin.

	Sphere	Cylinder	Cuboid
S_8	3.40 ± 0.86	3.84 ± 0.92	4.55 ± 0.44
S_9	2.82 ± 0.95	4.55 ± 0.87	4.76 ± 0.74
Mean	3.11 ± 0.91	4.20 ± 0.90	4.66 ± 0.59

Table 5. Table reporting mean effective diffusion coefficients and related standard deviations in $10^{-9}\ m^2/s$ for samples with $S/V = 7.41\ cm^{-1}$ $(\pm 5\%)$ fixed for $24h$ in neutral buffered formalin.

	Sphere	Cylinder	Cuboid
S_{10}	1.14 ± 0.39	1.84 ± 0.31	2.27 ± 0.28
S_{11}	1.17 ± 0.34	2.06 ± 0.35	2.17 ± 0.24
Mean	1.16 ± 0.37	1.95 ± 0.33	2.22 ± 0.26

Table 6. Table reporting mean effective diffusion coefficients and related standard deviations in $10^{-9}\ m^2/s$ for sample with $S/V = 7.41\ cm^{-1}$ $(\pm 5\%)$ fixed for $48h$ in neutral buffered formalin.

	Sphere	Cylinder	Cuboid
S_{10}	1.16 ± 0.38	1.78 ± 0.22	2.06 ± 0.26
S_{11}	1.35 ± 0.40	1.66 ± 0.39	1.93 ± 0.28
Mean	1.26 ± 0.39	1.72 ± 0.31	2.00 ± 0.27

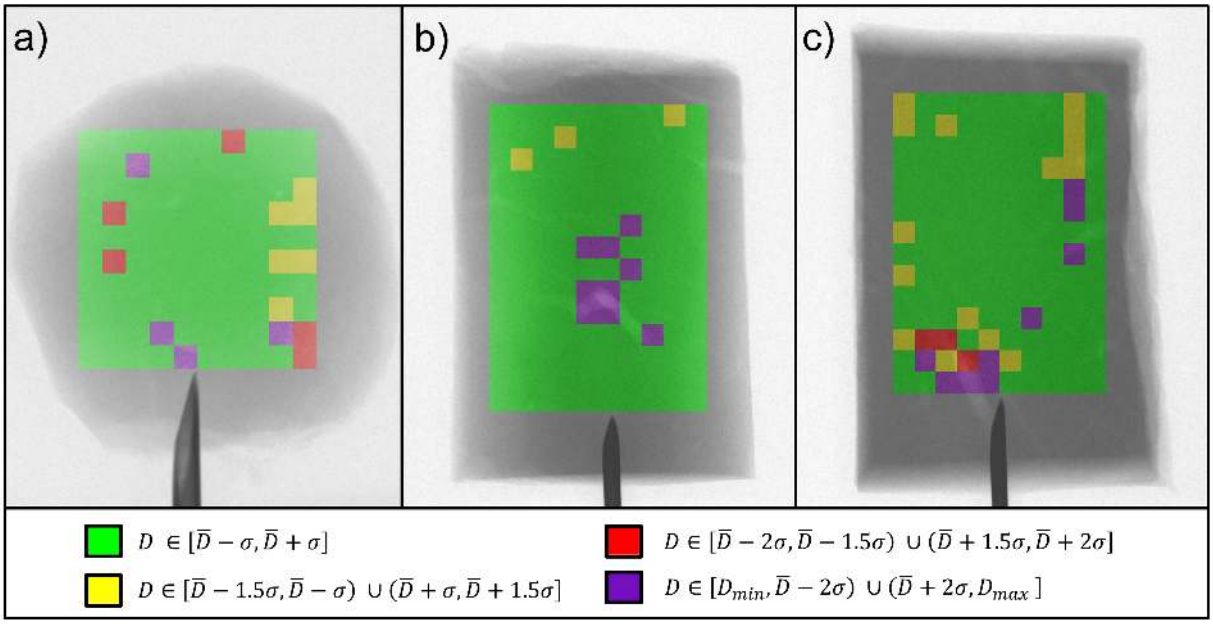

Figure 5. The figure illustrates color maps obtained for three samples: a) spherical, b) cylindrical and c) cuboid-shaped. At the bottom the related legend is reported.

4. Discussions

The effective diffusion coefficient estimates were analyzed in relation to room temperature fluctuations, V_{sam}/V_{sol} ratio, and samples S/V ratio. In the ranges of the analysis, no significant relationships were found with respect to both temperature and V_{sam}/V_{sol} ratio (down to $1:25$). Instead, a significant dependence of the D_{eff} on the sample S/V ratio was identified (Fig. (6)). In particular, the effective diffusion coefficient decreases non-linearly as the S/V ratio increases, a trend observable in each of the three geometries analyzed. The shape of the specimen also influences the D_{eff} estimates, with higher values found for cuboid-shaped samples and lower values found for spherical samples. These behaviors are probably related to differences in natural convective mass transfer processes at the sample surface, which depend on the geometric shape of the sample.
Regarding the D_{eff} estimates within each sample, samples are in general characterized by uniform diffusion coefficients, as evidenced by the extended green zones in each sample in Fig. (5). The irregular nature of the biological tissues, including structural and compositional heterogeneity and vascularity, yields different diffusion coefficients, which are identified as yellow, red, and purple zones in Fig. (5). These findings highlight the capability of the method to identify structural and compositional tissue inhomogeneities, particularly those related to modified tissue diffusivity.

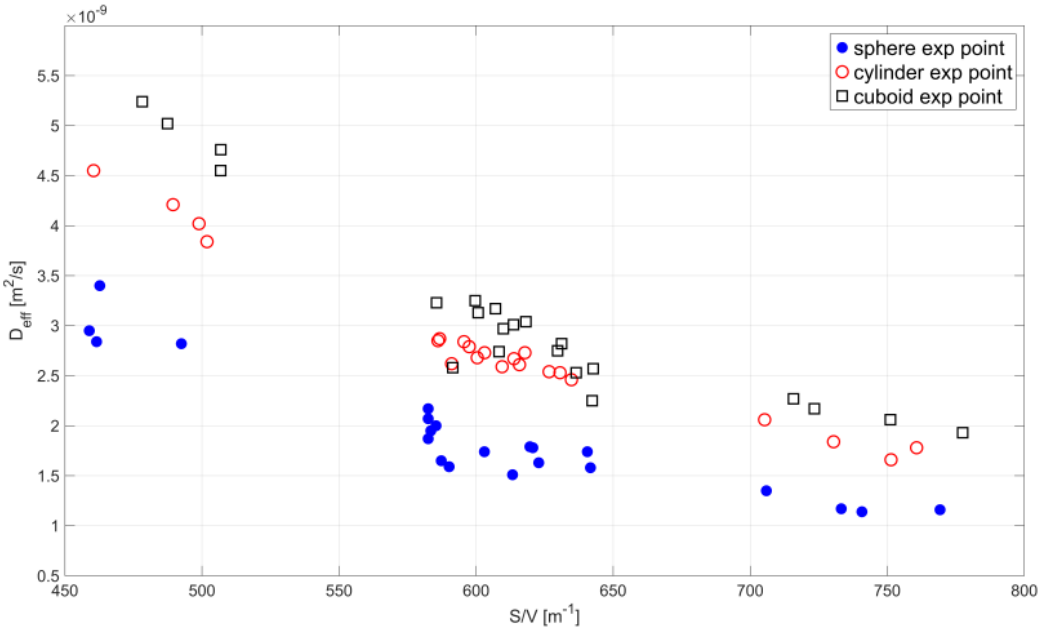

Figure 6. The figure shows the relationship between estimated D_{eff} in m^2/s and S/V in m^{-1} for the three geometries considered.

5. Conclusions

The presented technique, which is based on the acquisition of time-series of radiographic images of histological samples submerged in a processing solvent, can be efficiently used to estimate diffusion coefficients in biological samples with different shapes and geometrical features. In particular, the estimation can be easily performed using samples of the three main geometries for histological resections, by sample immersion, radiographic acquisition, and calculation of the effective diffusion coefficient via a fast and simple post-processing code. The D_{eff} estimates have demonstrated a dependence on both geometric shape and the S/V ratio, which requires further investigation in upcoming works. In general, this technique, which is pragmatic and readily engineerable, can be efficiently implemented in the future to improve histological sample processing and achieve precise, fast, and accurate medical diagnosis.

Acknowledgements

This work was funded by the Italian National Plan for NRRP Complementary Investments (PNC), established with the decree-law 6 May 2021, n. 59, converted by law n. 101 of 2021 in the call for the funding of research initiatives for technologies and innovative trajectories in the health and care sectors (Directorial Decree n. 931 of 06/06/2022). Project n. PNC0000003 "AdvaNced Technologies for Human-centrEd Medicine" acronym: ANTHEM.

References

Agrawal, L., Engel, K. B., Greytak, S. R., & Moore, H. M. (2018). Understanding preanalytical variables and their effects on clinical biomarkers of oncology and immunotherapy. In *Seminars in cancer biology* (Vol. 52, pp. 26–38).

Bauer, D. R., Stevens, B., Chafin, D., Theiss, A. P., & Otter, M. (2016). Active monitoring of formaldehyde diffusion into histological tissues with digital acoustic interferometry. *Journal of Medical Imaging*, *3*(1), 017002–017002.

Crank, J. (1979). *The mathematics of diffusion*. Oxford university press.

Ekundina, V., & Eze, G. (2015). Common artifacts and remedies in histopathology (a review). *African Journal of Cellular Pathology*, 1–7.

Engel, K. B., & Moore, H. M. (2011). Effects of preanalytical variables on the detection of proteins by immunohistochemistry in formalin-fixed, paraffin-embedded tissue. *Archives of pathology & laboratory medicine*, *135*(5), 537–543.

Kokkat, T. J., Patel, M. S., McGarvey, D., LiVolsi, V. A., & Baloch, Z. W. (2013). Archived formalin-fixed paraffin-embedded (ffpe) blocks: a valuable underexploited resource for extraction of dna, rna, and protein. *Biopreservation and biobanking*, *11*(2), 101–106.

Le Houx, J., Ruiz, S., McKay Fletcher, D., Ahmed, S., & Roose, T. (2023). Statistical effective diffusivity estimation in porous media using an integrated on-site imaging workflow for synchrotron users. *Transport in Porous Media*, *150*(1), 71–88.

Lerch, M. L., Bauer, D. R., Chafin, D., Theiss, A., Otter, M., & Baird, G. S. (2017). Precision medicine starts with preanalytics: Real-time assessment of tissue fixation quality by ultrasound time-of-flight analysis. *Applied Immunohistochemistry & Molecular Morphology*, *25*(3), 160–167.

Lerch, M. L., Bauer, D. R., Theiss, A., Chafin, D., Otter, M., & Baird, G. S. (2019). Monitoring dehydration and clearing in tissue processing for high-quality clinical pathology. *Biopreservation and biobanking*, *17*(4), 303–311.

Luikov, A. (2012). *Analytical heat diffusion theory*. Elsevier.

Magaki, S., Hojat, S. A., Wei, B., So, A., & Yong, W. H. (2018). An introduction to the performance of immunohistochemistry. *Biobanking: methods and protocols*, 289–298.

Mai, H., & Lu, D. (2024). Tissue clearing and its applications in human tissues: a review. *View*, *5*(2), 20230046.

McInnes, E. (2005). Artefacts in histopathology. *Comparative Clinical Pathology*, *13*(3), 100–108.

Olver, F. W. (2010). *Nist handbook of mathematical functions*. Cambridge University Press, Cambridge.

P. D. Moon, E. S. (1988). *Field theory handbook* (Second ed.). Springer-Verlag.

Posnansky, O., & Shah, N. (2008). On the problem of diffusivity in heterogeneous biological materials with random structure. *Journal of biological physics*, *34*(6), 551–567.

Santini, M., Fest-Santini, S., Cossali, G., Casatta, N., & Lupo, C. (2023). *Sistema e metodo per la processazione di campioni biologici (deposito della domanda di brevetto n. 102023000019599).* deposito della domanda di brevetto n. 102023000019599.

Santini, M., Fest-Santini, S., Cossali, G., Casatta, N., & Lupo, C. (2024). A novel methodology for the diffusion coefficient determination in porous media by x-ray high-resolution radiographies. *The European Physical Journal Plus*, *139*(8), 1–7.

Santini, M., Guilizzoni, M., & Fest-Santini, S. (2013). X-ray computed microtomography for drop shape analysis and contact angle measurement. *Journal of colloid and interface science*, *409*, 204–210.

Sen, P. N., & Basser, P. J. (2005). A model for diffusion in white matter in the brain. *Biophysical journal*, *89*(5), 2927–2938.

Spencer, L., Bancroft, J., & Gamble, M. (2012). Tissue processing. In *Bancroft's theory and practice of histological techniques. 7nd ed.* (pp. 105–23). Elsevier Health Sciences.

Taqi, S. A., Sami, S. A., Sami, L. B., & Zaki, S. A. (2018). A review of artifacts in histopathology. *Journal of oral and maxillofacial pathology*, *22*(2), 279.

Villanacci, V., Reggiani-Bonetti, L., Caprioli, F., Saragoni, L., Salviato, T., Mescoli, C., … others (2020). Histopathology of inflammatory bowel disease—position statement of the pathologists of the italian group for the study of inflammatory bowel disease (ig-ibd) and italian group of gastrointestinal pathologists (gipad-siapec). *Digestive and Liver Disease*, *52*(3), 262–267.

Zhu, L., Zhang, H., Gu, H., & Zhou, J. (2024). The pathology biopsy represents the "gold standard" for diagnosis: a case report. *Diagnostic Microbiology and Infectious Disease*, *108*(2), 116138.